Available online at www.sciencedirect.com
SCIENCE DIRECT®
Journal of Membrane Science 232 (2004) 19–30
journal of MEMBRANE SCIENCE
www.elsevier.com/locate/memsci

Experimental validation of CFD mass transfer simulations in flat channels with non-woven net spacers

F. Li*, W. Meindersma, A.B. de Haan, T. Reith

Department of Chemical Engineering, University of Twente, P.O. Box 217, 7500 AE Enschede, The Netherlands

Received 16 December 2002; received in revised form 13 November 2003; accepted 20 November 2003

Abstract

The objective of the present paper is to validate experimentally the mass transfer simulations presented in a previous paper by the same authors [J. Membr. Sci. 208 (2002) 289]. In the present study, mass transfer coefficients were obtained by the limiting current method.

The results from CFD simulations were successfully validated by experiments. The experiments confirm that the geometric parameters of spacers have a considerable influence on mass transfer at a given cross-flow power consumption. Comparison of the experiments with different non-woven spacers shows that there is an optimal spacer geometry, which agrees with those of the optimal spacer obtained by CFD simulations. The experiments also indicate that the woven and non-woven spacers perform equally well. Since all commercial net spacers investigated in this study had non-optimal spacer geometries, they showed lower mass transfer coefficients at a given cross-flow power consumption than the optimal spacer.

Keywords: Spiral wound membrane module; Spacer; Mass transfer; Limiting current method; CFD

1. Introduction

Membrane filtration covers a wide range of separations ranging from filtration of solids to molecular separations. A common phenomenon in many of those processes is concentration polarization, due to accumulation of rejected particles/molecules at the membrane. Concentration polarization lowers flux and quality of the permeate. Different hydrodynamic approaches have been used for suppressing concentration polarization. For instance, the geometry of feed spacers in spiral wound membrane modules, which has primarily a support function, can be modified for the purpose of enhancing back-mixing of the rejected species to the bulk of the feed flow. However, such spacer modifications will generally lead to more cross-flow power consumption in the channel. Therefore, there is a trade-off between enhanced mass transfer and increased cross-flow power consumption. The performance of feed spacers in terms of mass transfer enhancement and cross-flow power consumption has been studied experimentally in the past decades [1–7]. These studies show that different methods have been used to optimize spacers. For instance, Da Costa et al. [8] carried out the optimization based on the relation between cost and flow rate, and in the study of Shen and Probstein [9], the relation between the Sherwood number (*Sh*) and the Reynolds number (*Re*) was used to optimize the geometry of spacers.

Since the late 1990s, computational fluid dynamics (CFD) has been used to investigate the flow phenomena in flat channels equipped with spacers [10–13]. The study by Li et al. [14] shows that CFD is a powerful tool to optimize non-woven spacers. However, CFD results have to be validated experimentally because of discretization and modeling errors [15].

In the previous paper [14] of the authors CFD simulation studies were reported on the optimization of spacers by the method of enhancing mass transfer in spiral wound modules for ultrafiltration. Various non-woven spacer geometries were compared in terms of dimensionless Sherwood numbers (*Sh*) and power numbers (*Pn*), where the power number (*Pn*) represents the cross-flow power consumption. The present paper focuses on the experimental validation of these CFD simulation studies. In Section 4 the method of optimization is summarized.

* Corresponding author. Tel.: +31-53-489-5447; fax: +31-53-489-4821.
E-mail address: f.li@ct.utwente.nl (F. Li).

0376-7388/$ – see front matter © 2003 Elsevier B.V. All rights reserved.
doi:10.1016/j.memsci.2003.11.015

The power number can be easily obtained from pressure drop measurements over a certain length of the spacer-filled channel with a differential pressure gauge.

The filtration method and limiting current method have been reported in literature as techniques for measurement of mass transfer coefficients in spacer-filled channels [3,5]. In the filtration method, mass transfer coefficients are calculated from the permeate flux by fitting the concentration polarization model to the measured fluxes [16]. This is a straightforward and well-known method often used by the membrane community. However, the filtration method proved to result in unreliable values of mass transfer coefficients [3]. On the basis of the above considerations, the limiting current method has been selected as the more reliable experimental technique. Since the permeation flux through the membrane is zero for both CFD simulations and for the limiting current method, a direct comparison between the simulated and measured mass transfer coefficients is allowed. The principle of the limiting current method is presented in the next section.

The permeation through porous channel walls such as membranes can have a major influence on mass transfer rates. Analytical solutions of mass transfer equations in empty porous channels report that mass transfer coefficients under permeation conditions are larger than those under non-permeation conditions [28–30]. A systematic study of the influence of permeation rate on mass transfer in spacer-filled channels has not been found in the literature. These observations do not imply that studies into mass transfer at non-permeation conditions do not make sense. On the contrary, these mass transfer coefficients are the starting point for further investigations into mass transfer in spacer-filled channels under permeation conditions.

In the previous publication of the authors [14] it was shown by CFD simulations that an optimal non-woven spacer does exist. The present paper will focus on the experimental validation of the CFD results in the following terms:

- Are flow and mass transfer “periodic fully developed” in the spacer-filled channel?
- Do the CFD results agree with the experimental results and do we find the same optimal spacer?
- Is the performance of commercial net spacers different from the optimal non-woven net spacer?

The experimental study was carried out in the Reynolds number range $Re = 100$–500, the same as for the CFD optimization study [14].

2. Description of the limiting current method

In the present study measurements of mass transfer from the bulk of the liquid flow to the walls of flat channels have been carried out with the limiting current method. This method has been validated by Selman and Tobias [17]. Applications of the method to the measurements of mass transfer in geometries relevant to membrane module design can be found in the work of Futselaar [18], Moulin [19], Feron [5] and others. For a more in-depth study of the limiting current method the reader is referred to the literature [20–23].

The limiting current method is schematically shown in Fig. 1. The cathode is used as the measuring electrode, and the anode is used as the counter electrode. The cathode and anode form part of the walls of the flat channel. The electrolyte solution flowing through the flow channel consists of a mixture of 0.001 M potassium ferricyanide ($K_3Fe(CN)_6$), 0.005 M potassium ferrocyanide ($K_4Fe(CN)_6$) and 0.5 M potassium nitrate (KNO_3) as supporting electrolyte in demineralized tap water. The anode area is considerably larger than the cathode area. A potential difference between the cathode and anode generates a current i in the cathode–anode circuit. Ferricyanide ions are reduced to ferrocyanide ions at the cathode and ferrocyanide ions are oxidized to ferricyanide ions at the anode. The current i is measured as a function of the potential difference ΔV between the cathode and the reference electrode in the liquid flow. The potassium nitrate is a supporting non-reactive electrolyte, which is added to increase the electrolyte conductivity for suppressing ion migration and reducing ohmic losses (Fig. 2).

The ion flux to the cathode is the combined result of migration (due to potential gradients), diffusion (due to concentration gradients) and convection (due to liquid flow) of the ions. Since potential gradients are negligible due to the supporting electrolyte and the liquid velocity is zero at the

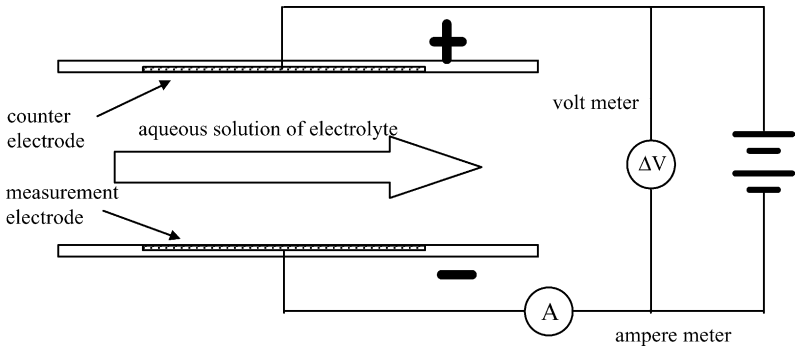

Fig. 1. Measurement channel with limiting current method.

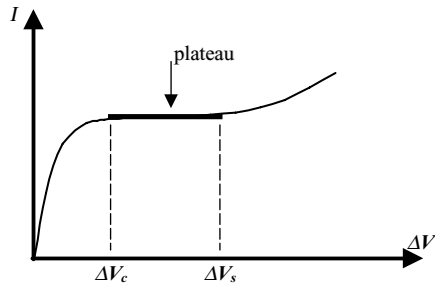

Fig. 2. Relation between current and potential difference in a redox system.

cathode surface, the ion flux to the cathode is totally controlled by ion diffusion. The local current density i at the cathode (A/m^2) is now described by Eq. (1):

$$i = nF\mathcal{D}\left.\frac{\partial C}{\partial y}\right|_{y=0} = nFk(C_b - C_c) \quad (1)$$

where n is the number of electrons of the ferricyanide ion participating in the reaction (here n=1), F the Faraday's constant, k the local mass transfer coefficient, $\mathcal{D}$ the diffusivity of the ferricyanide ions, C_b the concentration of the ferricyanide in the bulk electrolyte, C_c the local concentration of the ferricyanide on the cathode surface and y the spatial coordinate perpendicular to the electrode surface. It should be noted that by definition k in Eq. (1) should be related to the mean cup concentration C_m. Since the thickness of the mass transfer boundary layer is small compared to the height of channels, C_m is commonly replaced by C_b, which simplifies calculations.

The total current through the cathode I is calculated by integrating the current density i over the measurement electrode area (A)

$$I = \int_A i\,\mathrm{d}A = nF\int_A (C_b - C_c)k\,\mathrm{d}A \quad (2)$$

Increasing the current I by raising the potential difference ΔV over the cathode, results in depletion of ferricyanide ions adjacent to the cathode surface. When the ferricyanide concentration at the cathode falls to zero or $C_c = 0$, Eq. (2) reduces to the expression for the limiting current I_{lim}:

$$I_{lim} = nFC_b\int_A k\,\mathrm{d}A = nFC_bA\bar{k} \quad (3)$$

In Eq. (3) $\bar{k}$ is the mean mass transfer coefficient on the area of the measurement electrode, defined as

$$\bar{k} \equiv \frac{1}{A}\int_A k\,\mathrm{d}A \quad (4)$$

According to Eq. (3) a further increase in potential difference ΔV does not result in an increased current: the cathode operates in the 'limiting current' or 'plateau' mode. When the potential difference is raised above ΔV_s, side reactions occur in the system resulting in higher currents.

The mean mass transfer coefficient $\bar{k}$ follows from Eq. (3):

$$\bar{k} = \frac{I_{lim}}{nFC_bA} \quad (5)$$

Eq. (5) relates the limiting current I_{lim} through the electrodes directly to the mean mass transfer coefficient $\bar{k}$ at the cathode, since all other quantities in Eq. (5) are known and constant quantities.

3. Experimental

3.1. Experimental setup

The experimental set up is shown in Fig. 3. The tank (volume of ca. 7 l) is equipped with a nitrogen sparger and a coiled heat exchanger fed by a thermostatted bath (Julabo F32.MW). The flow is generated by one of the parallel mounted gear pumps P1 and P2 (Verder type V096.07P and

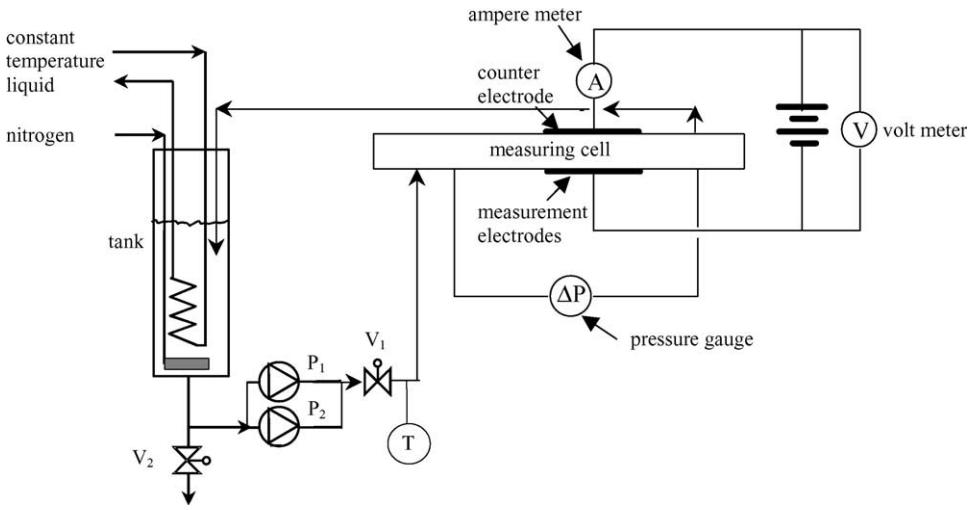

Fig. 3. The experimental setup.

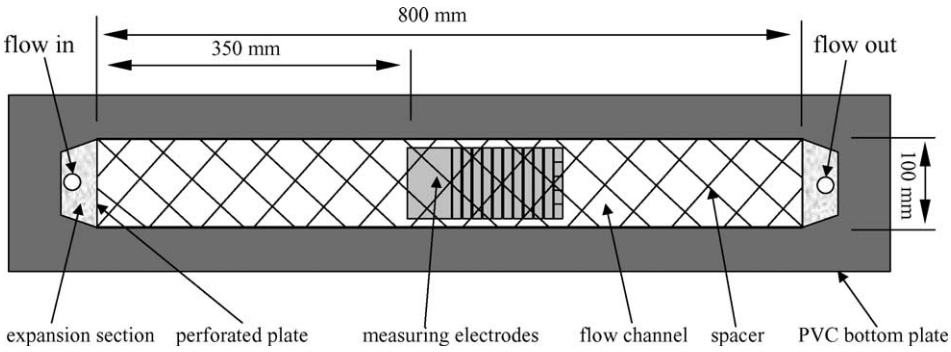

Fig. 4. View on the lower wall of the flow channel with measuring electrodes.

V5K.P) depending on the desired flow rate, which can be read from a flow meter (Endress + Hauser Progma A).

The measuring flow channel consists of a top and a bottom plate separated by PVC O-rings with adjustable heights from 1 to 6 mm. Details of the bottom plate of the measuring channel are shown in Fig. 4. The channel length is 800 mm and the channel width is 100 mm. The flow enters at the left side of the channel through an expansion section and a perforated plate for flow distribution. The hydraulic entrance length in the empty channel in present study is always less than 350 mm, which means that the flow entering the measuring section is always a fully-developed laminar flow. The spacer material under investigation is inserted between the top and bottom plates (see Fig. 4).

The pressure drop over a distance of 350 mm was measured with a differential pressure gauge (Honeywell ST3000). The current was read from an ampere meter. The flow system is equipped with de-aeration devices at the appropriate points. The whole set up is placed in a shielded box (1.8 m × 1.0 m × 0.75 m) to avoid degradation of the electrolyte by light.

The measurement electrodes as shown in Fig. 5 consist of one large electrode (50 mm × 80 mm), 10 medium-sized electrodes (10 mm × 80 mm) and five small electrodes (10 mm × 16 mm). The electrodes are cut from platinum sheets of 1 mm thickness. The size of the counter electrode is 200 mm × 100 mm. In plastic sheets channels with the same height and width as the platinum electrode strips are milled in which the electrodes are glued. The distance between the electrode strips (in the flow direction) is ca. 0.2 mm, providing electrical insulation between the strips. Afterwards the electrode surfaces are smoothened and polished. The plastic sheets are again glued on the walls of the measuring channel. All electrodes are connected with pin switches so that different electrode combinations can be formed. This arrangement enables observation of the development of the mass transfer boundary layer.

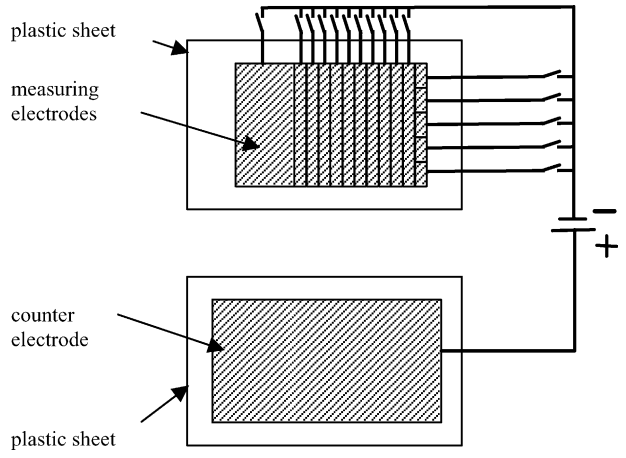

Fig. 5. The configuration of electrodes.

Many mass transfer studies reported in literature are based on the use of nickel or gold electrodes. However, the reliability and reproducibility of the measurements carried out with these electrodes appeared to be questionable [24,25], probably due to the occurrence of side reactions. Application of platinum electrodes resulted in reliable and reproducible measurements.

The pumps and all metal surfaces in the flow circuit are connected to earth, while the electrode measuring circuit is insulated from earth (floating).

The existence of oxygen in solution can cause side reactions resulting in erroneously high limiting currents. Before starting an experimental run, the circulating solution needs to be sparged continuously with nitrogen for at least 1 h. During the experiments sparging of the solution should be continued.

All measurements were carried out with temperature at 20 ± 0.2 °C.

3.2. Physical properties of the solution

The physical properties of the solution are dependent on temperature. Due to limited availability of relevant literature data, density and viscosity of the electrolyte liquids were measured in the laboratory. Relevant physical parameters at 20 °C are shown in Table 1.

The diffusivity of $[Fe(CN)_6]^{3-}$ is predicted with the Stokes–Einstein equation [26,27]:

$$\frac{\mathcal{D}\mu}{T} = 2.50 \times 10^{-15} \quad (6)$$

Table 1
Physical properties of the electrolyte solutions

Temperature (°C)	20
Density (kg/m^3)	1034
Kinematic viscosity (m^2/s)	0.9764×10^{-6}
Diffusivity[a] (m^2/s)	7.260×10^{-10}

[a] Diffusivity of the $[Fe(CN)_6]^{3-}$ ions.

Table 2
Composition of electrolyte solutions

Solution	KNO_3 (M)	$K_3[Fe(CN)_6]$ (M)	$K_4[Fe(CN)_6]$ (M)
1	0.5	0.001	0.005
2[a]	0.5	0.0005	0.0025

[a] Only for measurements at high Reynolds numbers.

In Eq. (6) $\mathcal{D}$ is the diffusivity of $[Fe(CN)_6]^{3-}$ ions in the solution, μ the dynamic viscosity of the solution and T the absolute temperature.

Higher Reynolds numbers lead to higher current densities (see Fig. 7) resulting in side reactions. Therefore, the measurements at higher Reynolds numbers were carried out with electrolytes with lower $K_3[Fe(CN)_6]$ and $K_4[Fe(CN)_6]$ concentrations as shown in Table 2. Since the concentrations of $K_3[Fe(CN)_6]$ and $K_4[Fe(CN)_6]$ are much smaller than the KNO_3 concentrations, densities and viscosities of the two electrolytic solutions are equal.

3.3. Geometric parameters of spacers

In Fig. 6, the geometric characterization of the investigated non-woven net spacers is shown schematically. All filaments of the symmetrical non-woven spacers studied in this work have the same diameter, which is equal to half the channel height (h/2) while the filament spacing is constant ($l_1 = l_2 = l$). Therefore, the geometric parameters l/h, α and β describe the geometry of the spacer completely.

For the experimental investigations non-woven spacers with different geometric parameters were put together in the laboratory. The dimensionless geometric parameters of these spacers are equal to those used in the CFD simulations, but the characteristic lengths (channel heights) are different (see Table 3).

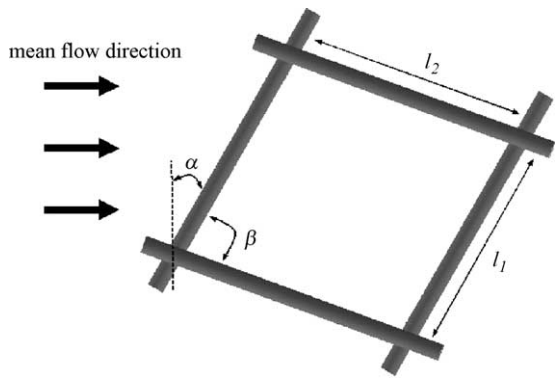

Fig. 6. Geometric characterization of a non-woven spacer.

Table 3
Geometric parameters of non-woven spacers

Number	h (mm)	l/h	α (°)	β (°)
1	6.0	2.2	0	90
2	4.0	4	0	90
3	4.0	4	45	90
4	4.0	4	30	120
5	4.0	4	60	60

Table 4
Geometric parameters of commercial spacers

Number	Brand	h (mm)	l/h	α (°)	β (°)	Type
C1	Naltex (39-4048)	3.0	3.1	52.5	75	Non-woven
C2	Naltex (39-4048)	3.0	3.1	37.5	105	Non-woven
C3	Nybolt (PA-4000/64)	1.9	2.8	0	90	Woven
C4	Nybolt (PA-4000/64)	1.9	2.8	45	90	Woven

Also a limited number of commercial spacers were investigated experimentally. For this purpose pieces of non-woven and woven commercial spacers fitting the flow channel were cut out from sheets of commercial spacers. The non-woven commercial spacer was provided by Naltex (39-4048), and the woven commercial spacer was from Nybolt (PA-4000/64). The geometric parameters of these commercial spacers are presented in Table 4.

4. Optimization of spacer geometry in a Sherwood–power number plot

In the previous paper [14] of the authors and in the present paper evaluation of spacer performance and optimization of spacer geometry is based on the comparison of two parameters: the consumption of cross-flow mechanical (pumping) power per unit volume of spacer SPC and the product of mass transfer coefficient and mass transfer area (wall or membrane area) per unit volume of spacer SKA. Spacers with a higher SKA per SPC are more efficient. In order to facilitate this comparison, the parameters SKA and SPC are incorporated in the dimensionless Sherwood numbers Sh and power numbers Pn, respectively, and the comparison and optimization are carried out in a Sh versus Pn plot.

Mass transfer and cross-flow power consumption in geometrically similar spacers can be analyzed by dimensional analysis as shown by the authors in the previous paper [14]. The results are summarized by Eq. (7):

$$Sh = F\left(Pn, Sc, \frac{l}{h}, \alpha, \beta\right) \tag{7}$$

In Eq. (7), Sh ($\equiv kh/\mathcal{D}$) is the Sherwood number, Sc ($\equiv \mu/\rho\mathcal{D}$) the Schmidt number and Pn ($=\mathrm{SPC}(\rho^2 h^4/\mu^3)$) the power number. SPC ($\equiv \Delta P\, \Phi_v/Lwh = \Delta P\, uwh/Lwh = (\Delta P/L)u$) is the cross-flow power consumption per unit volume of spacer-filled channel and the Sh number can

be written as: $Sh \equiv kh/\mathcal{D} = (kLw/Lwh)(h^2/\mathcal{D}) = \mathrm{SKA}(h^2/\mathcal{D})$ in which SKA ($=kLw/Lwh$) is the product of mass transfer coefficient and membrane (wall) area per unit volume of spacer-filled channel.

The geometry of the non-woven net spacers used in the present investigation is characterized by three dimensionless parameters: l/h, α and β, in which h is the channel height, l the filament spacing, α the flow attack angle, and β the angle between crossing filaments. The diameter of the filaments is half the channel height, therefore, not an independent relevant variable. More complicated spacer geometries, as asymmetric spacers and multilayer spacers, have to be characterized by more than three dimensionless parameters.

In order to transform the geometric length variables of a spacer geometry to dimensionless geometric parameters, all length variables are expressed as fractions (or multiples) of one of the length variables. In textbooks on dimensional analysis [31], this length variable is known as the characteristic length of the spacer geometry. The characteristic length does not specify the complete spacer geometry, but only its size. As explained above, a complete geometric specification contains all relevant geometric parameters. Therefore, this characteristic length should not be confused with the hydraulic diameter of the spacer-filled channels, which is used in the Fanning equation for pressure drop calculations of turbulent flows in non-circular ducts and channels. The different nature of the hydraulic diameter d_h can easily be deducted from its definition: $d_h \equiv (4 \times \text{area of channel cross-section})/(\text{wetted perimeter})$. Since the geometric parameters specify the spacer geometry completely, the introduction of more geometric parameters as voidage and hydraulic diameter would obscure a proper application of dimensional analysis.

Several authors a.o. Schock and Miquel [1], Da Costa et al. [8] and Belfort and Guter [32] have used the hydraulic diameter and spacer voidage for characterizing the spacer geometry in their modeling studies of power consumption and mass transfer in empty and spacer-filled channels. The present study, however, focuses on spacer geometry optimization by CFD simulation and experimentation, for which such modeling of flow and mass transfer mechanisms in the spacer-filled channels is not needed.

Dimensional analysis allows the choice of any length of the spacer geometry as characteristic length: channel height, radius of the filaments or filament spacing. However, the channel height h is the most practical choice, since it enables comparison of the SKA values of various spacer geometries at the same specific cross-flow power consumption SPC in the same channel and, consequently, at the same channel height h.

The above analysis shows that all values of Sh for geometrically similar spacers fall on a single curve in a Sh versus Pn plot. Each different geometry, however, leads to a different single curve in this plot.

The above dimensional analysis is of vital importance for the present work, since it reduces the number of simulations and experimental effort and allows scaling-up and scaling-down of the results of simulations and experiments. Especially, the latter is important, since it allows, e.g. downscaling of the optimal spacer geometry determined at a channel height $h = 4$ mm to a geometrically similar optimal spacer with a more realistic industrial scale of 1–2 mm.

5. Results and discussions

5.1. Calibration of the setup

The setup was calibrated by comparing experimental Sh and Pn values determined in fully laminar flows in the empty channel with a height of 5 mm with values predicted by theory.

Fig. 7 shows the expected current plateaus at three different Reynolds numbers.

Comprehensive theoretical and experimental studies on the hydrodynamics and mass transfer in an empty flat channel have been reported in literature. The power number Pn and the Reynolds number Re for fully-developed laminar flow through empty channels are related as follows [14]:

$$Pn \equiv \mathrm{SPC}\frac{\rho^2 h^4}{\mu^3} = 12\,Re^2 \tag{8}$$

The well-known Graetz equation predicts the Sherwood numbers for developing mass transfer boundary layers in fully-developed laminar flow. For empty channels the relationship is

$$Sh_{\text{empty}} = 1.47\left(Re\,Sc\frac{h}{L}\right)^{1/3} \quad \text{for } Re\,Sc\frac{h}{L} > 20 \tag{9}$$

in which Sc is the Schmidt number, h the height of the channel and L the length of the mass transfer boundary layer in the flow direction. A theoretical Sh–Pn relationship is obtained by eliminating Re from Eqs. (8) and (9).

For the calibration experiments, the largest measuring electrode of 50 mm ($L_e/h = 10$) in the flow direction was used. The Pn versus Re and the Sh versus Pn plots in Figs. 8 and 9, respectively, show satisfactory agreement between measurements and theory.

5.2. Development of the mass transfer boundary layer in spacer-filled channels

The CFD simulations reported in the previous paper by the present authors [14] have been based on the assumption of "periodic fully-developed flow" after a few flow cells. This means that after a few flow cells the flow pattern in each flow cell is self-similar (repeating itself in each consecutive flow cell) and that, therefore, mass transfer in spacer-filled channels is also periodic fully-developed. This is a plausible assumption since channels with non-woven spacers consist of a large number of identical cells (see

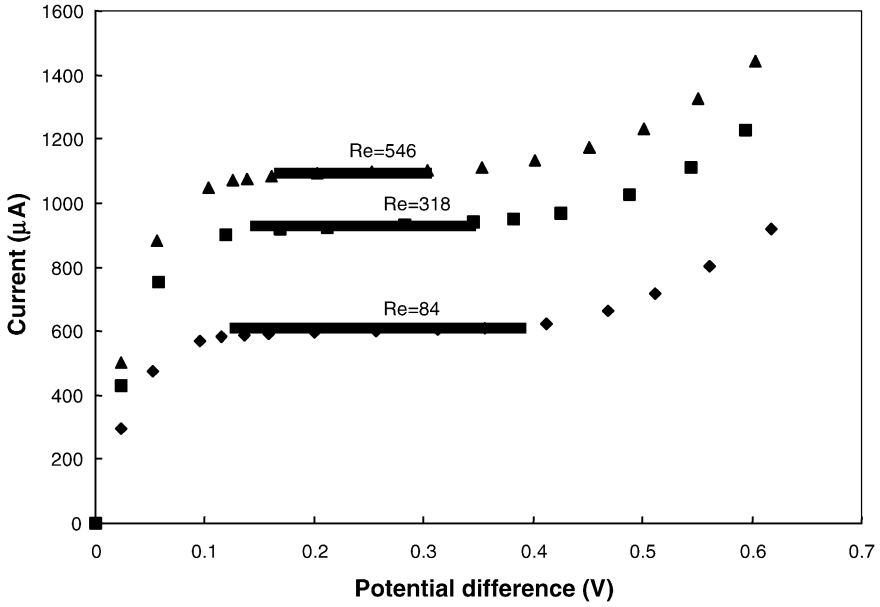

Fig. 7. The limiting current plateaus at different Reynolds numbers in the empty channel ($h = 5$ mm).

Fig. 6) with streamwise-periodic cross-sections. This assumption was checked in the present study by measuring mass transfer coefficients at increasing distances in the flow direction from the left edge of the large electrode. Fig. 10 shows the *Sh* numbers obtained from measurements with the various measuring electrodes in the flow direction (from left to right). In the same figure the positions of transversal spacer rods (circles) and the measuring electrodes (shaded strips) are indicated. Two sets of measurements are shown:

1. The spacer rods *perpendicular* to the mean flow direction are positioned at the wall with the measuring electrodes (triangles).
2. The spacer rods *parallel* to the mean flow direction are positioned at the wall with the measuring electrodes (squares).

The first set of measurements show considerable differences between the experimental *Sh* numbers. This is a direct consequence of the pronounced peaks in the mass transfer profiles in the flow cells [14] combined with the difference in spatial periodicity between the spacers and the measuring electrodes. The solid line in Fig. 10, showing the *Sh* values obtained by CFD simulations for fully-developed mass transfer, follows reasonably well the variations of the experimental *Sh* numbers, supporting the above argument. The

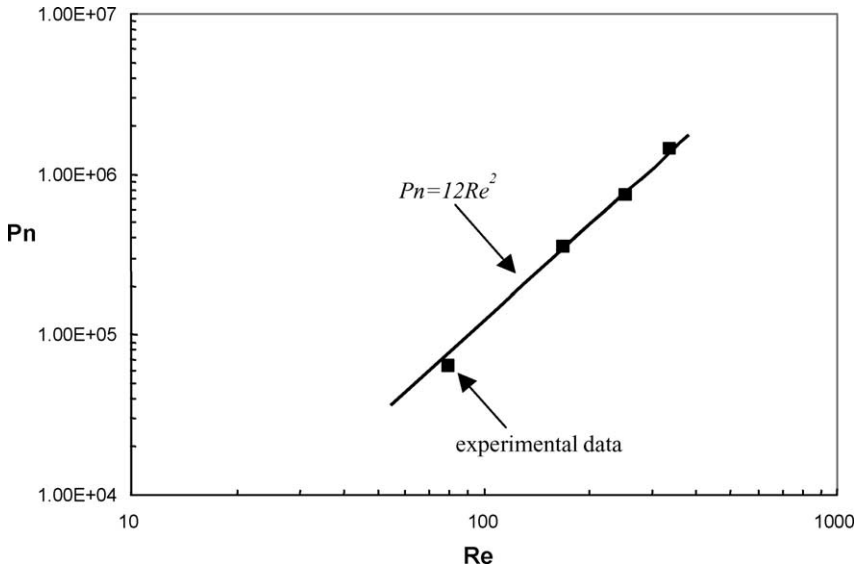

Fig. 8. *Pn* vs. *Re* plot for the empty channel ($h = 5$ mm, $L/h = 10$).

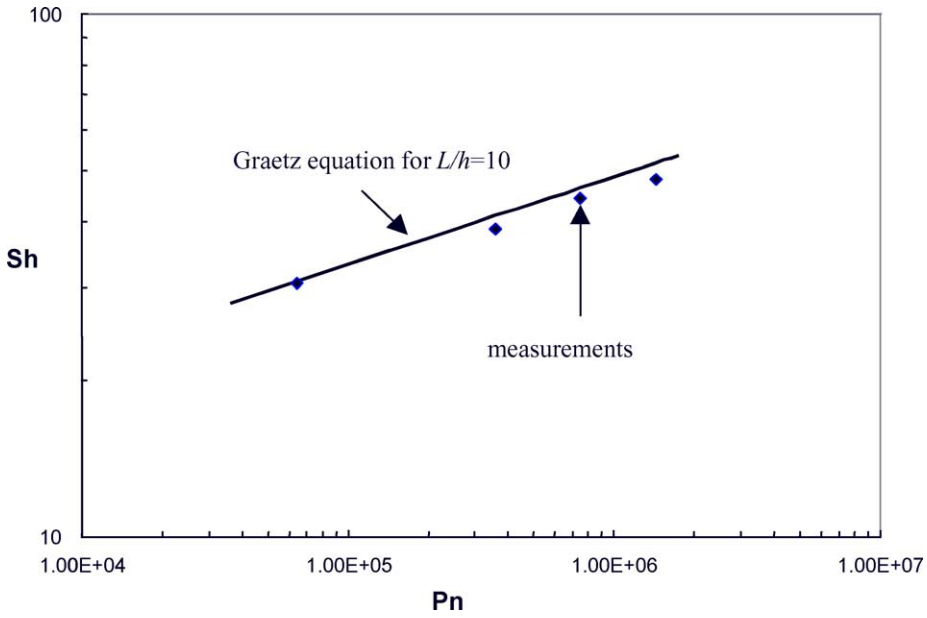

Fig. 9. *Sh* vs. *Pn* plot for the empty channel ($L/h = 10$).

second set of measurements does not show these large *Sh* variations, since the mass transfer profiles in the flow cells are rather smooth here. These observations imply that already after the first measuring electrode, whose size in the mean flow direction is equivalent to about three to five flow cells, the condition of periodic fully-developed mass transfer is satisfied.

Finally, it should be emphasized that the term "periodic fully-developed flow" is meant to specify the periodicity of the flow in the flow cells but not the hydrodynamics of the flow and mass transfer inside the spacer-filled channels. See Section 5.3 for remarks on the hydrodynamics of the flows.

5.3. Comparison between experiments and CFD simulations for non-woven spacers

As explained in Section 4, the performance of a spacer is characterized by its position in a *Sh* versus *Pn* plot.

The *Sh* numbers shown in the graphs are the arithmetic mean of the *Sh* numbers at the upper and lower walls of the channel. This means that the *Sh* numbers at either wall had to be determined separately for the spacers 1 and 2 in Table 3, while this was not necessary for the spacers 3–5 for symmetry reasons.

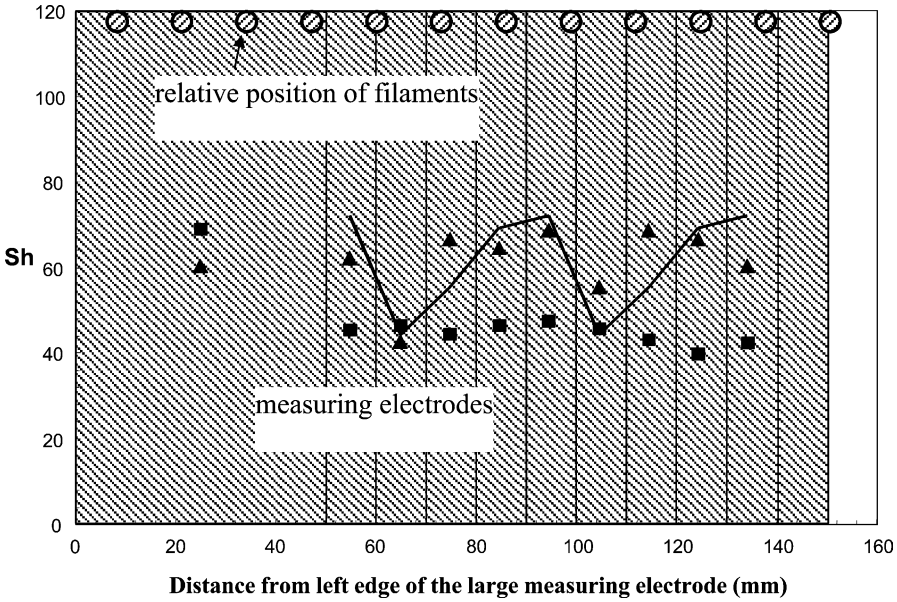

Fig. 10. *Sh* numbers measured at increasing distances from the left edge of the large electrode, $Re = 215$.

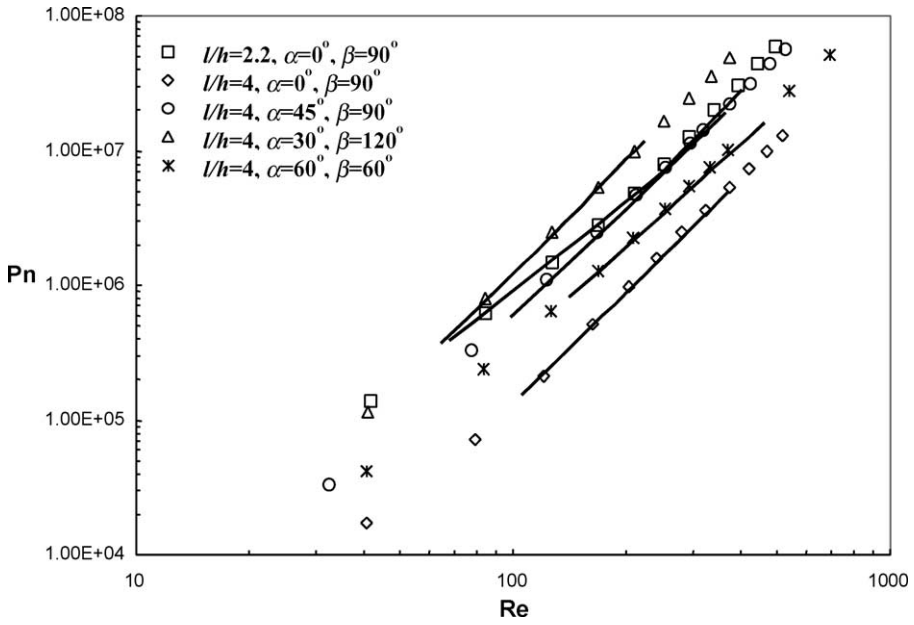

Fig. 11. *Pn* vs. *Re* plot for the spacers listed in Table 3.

Sh and *Pn* numbers were obtained experimentally for the non-woven spacers listed in Table 3 and compared with *Sh* and *Pn* numbers obtained for the same spacers by CFD calculations [14].

In the *Pn* versus *Re* plot in Fig. 11 experimental results are compared with results obtained by CFD simulations. Fig. 12 shows the *Sh* versus *Pn* plot for comparison of experimental and simulation *Sh* values. It can be seen from both figures that the agreement between experimental data and CFD simulations is satisfactory.

All geometric parameters have a marked influence on spacer performance, but the role of l/h is more significant than that of α and β. The optimal geometric parameters based on the present experimental study are $l/h = 4$, $\alpha = 30^\circ$ and $\beta = 120^\circ$ (spacer 4 in Table 3). Spacer optimization by CFD simulations resulted in the same geometric parameters.

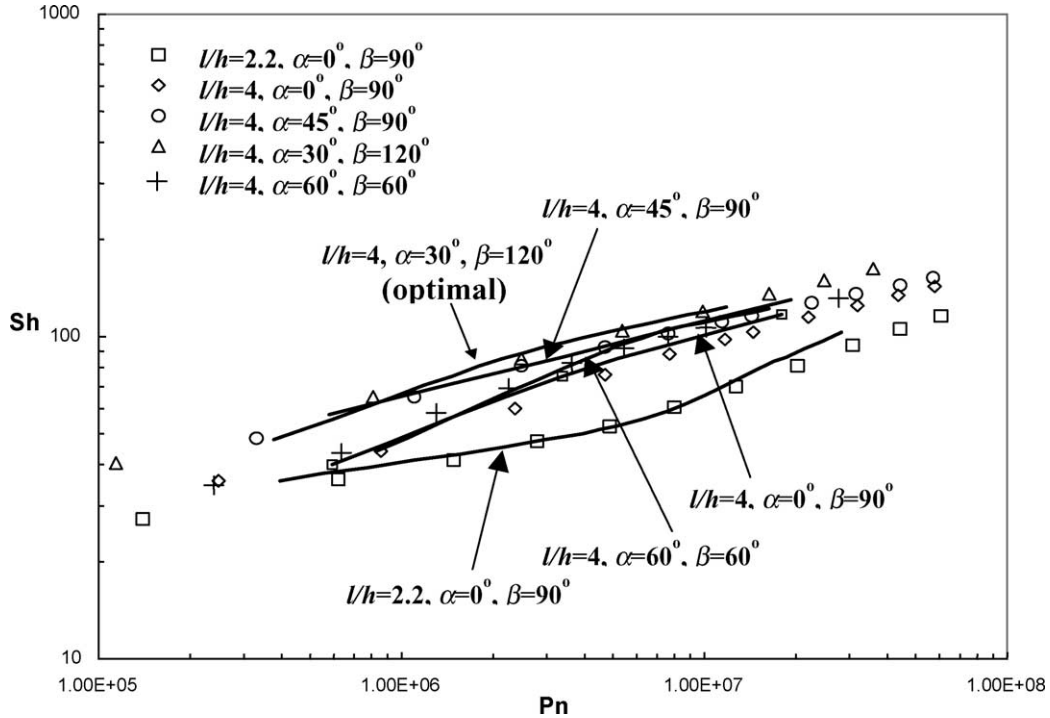

Fig. 12. *Sh* vs. *Pn* plot for the non-woven spacers listed in Table 3.

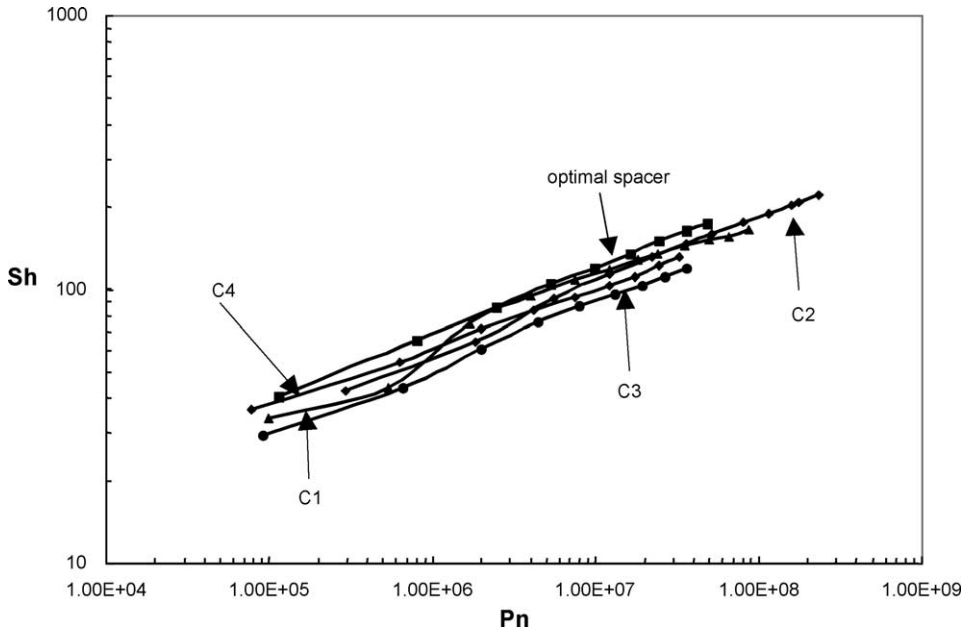

Fig. 13. *Sh* vs. *Pn* plot for comparison of the commercial spacers listed in Table 4 with the optimal spacer.

5.4. Performance of commercial spacers

The performance of the commercial spacers listed in Table 4 is shown in Fig. 13. The performance of non-woven and woven spacers seems to be similar, but definite conclusions are difficult to draw due to the differences between the geometric parameters and the limited number of commercial spacers investigated.

It is interesting to note that the performance of the investigated commercial spacers is sub-optimal, due to the fact that the geometric parameters of the commercial spacers differ from those of the optimal spacer. Their *l*/*h* ratios are about 3, which is lower than the optimal value of 4.

5.5. Flow and mass transfer in channels with non-woven net spacers

Flow and mass transfer are discussed here in terms of friction factors *f* and Sherwood numbers *Sh*, since the dependency of these dimensionless numbers on the Reynolds numbers *Re* may help to understand the underlying flow phenomena. See Da Costa et al. [8] for a more detailed analysis.

In the previous paper of the authors the Euler number *Eu* was introduced as $Eu \equiv \Delta P/\rho u^2$ and it was shown that for a given spacer geometry $f \propto Eu(h/L) \propto Eu$, where *f* is the well-known friction factor. Values of $Eu(h/L)$ as a function of *Re* can be easily deduced from the *Pn* versus *Re* plot in Fig. 11, where $Pn = \mathrm{SPC}(\rho^2 h^4/\mu^3) = (\Delta P/\rho u^2)(h/L)(\rho u h/\mu)^3 = Eu(h/L)Re^3$. Values of *Sh* as function of *Re* follow directly from the *Sh* versus *Pn* power plots and Fig. 11.

For a given spacer geometry and size, both the friction factor *f* and the Sherwood number *Sh* depend solely on the Reynolds number *Re*. It is customary to express these relationships in terms of power expressions: $f \propto Re^p$ and $Sh \propto Re^q$. In the present study, analysis of the experimental data in the range $100 < Re < 500$ indicates that the majority (all except 1) of the spacers have values of *p* in the range −0.5 to −0.25 and values of *q* in the range 0.6–0.7. The following cases are used as reference [33,34]:

(1) for fully turbulent flows in empty channels: $p = -0.25$ and $q = 0.8$;
(2) for flows around rods (vortex shedding): $p = -0.30$ and $q = 0.5$;
(3) for flows with developing boundary layers along flat plates: $p = -0.5$ and $q = 0.5$;
(4) for creeping (fully laminar) flows: $p = -1$ and $q = 0.33$.

The values of *p* and *q* in the cases 2 and 3 are for single cylindrical rod. Therefore, the difference between these values and that obtained from present study, i.e. *p* in the range −0.5 to −0.25 and values of *q* in the range 0.6–0.7 can be expected due to different flow patterns. For case 2, the mass transfer is mainly due to vortex shedding; for case 3, the mass transfer enhancement in comparison with case 1 is caused by developing mass transfer and hydrodynamic boundary layers. In spacer-filled channels, vortex shedding can be noticed at *Re* above 50–100 [14]. The filaments of spacers also periodically interrupt the development of the hydrodynamic and mass transfer boundary layers on the walls. The existence of both vortex shedding and periodic re-development of the mass transfer boundary layer can provide larger mass transfer enhancement than either case 2 or case 3. This can be seen from the values of *p* and *q* found in the present study. However, because the Reynolds number

is below 500 in present study, we cannot expect fully turbulent flow in spacer-filled channels. This is also shown by comparison the values of p and q from the present study and that presented in case 4. Da Costa et al. [18] measured values of p in the range -0.16 to -0.40 for various net spacers, which are not far from the values determined in the present investigation. Comparison of values of q determined under non-permeation conditions with those reported in literature under permeation conditions is not meaningful, since permeation has a considerable influence on Sh, as explained already in Section 1.

6. Conclusions

The major conclusions from the present study are summarized as follows:

(1) The results from CFD simulations were successfully validated by experiments. Close agreement was observed between simulations and experiments.
(2) The entry length in the channels with spacers is equivalent to about three to five repeated flow cells in the mean flow direction, much shorter than that in empty channels with the same channel height. Therefore, the entry effect in feed channels equipped with net spacers can be neglected.
(3) The performance of spacers is dependent on their geometric parameters. The geometric parameters of the optimal spacer are $l/h = 4, \alpha = 30^\circ$ and $\beta = 120^\circ$ (spacer 4), which are identical to those obtained by CFD simulations.
(4) The performance of woven and non-woven commercial spacers seems to be similar. The performance of the commercial spacers are sub-optimal, due to the fact that their geometric parameters differ from those of the optimal spacer.

Acknowledgements

The financial support of STW, the Dutch Technology Foundation, is gratefully acknowledged.

Nomenclature

A	area of measurement electrode (m^2)
C_b	bulk concentration of $[Fe(CN)_6]^{3-}$ in the solution (mol/m^3)
C_m	mean cup concentration of $[Fe(CN)_6]^{3-}$ in the solution (mol/m^3)
$\mathcal{D}$	diffusivity of $[Fe(CN)_6]^{3-}$ ions (m^2/s)
F	Faraday's constant (C/eq)
h	height of the channel (m)
k	mean mass transfer coefficient to the channel's wall (m/s)
l, l_1, l_2	filament spacing (m)
L	length of the channel filled with spacer (m)
L_e	length of the measuring electrode (m)
n	number of electrons participating in the reaction on the measuring electrodes
Pn	power number ($\equiv SPC(\rho^2 h^4/\mu^3)$)
ΔP	pressure difference over the channel (Pa)
Re	Reynolds number ($\equiv \rho u h/\mu$)
Sc	Schmidt number ($\equiv \mu/\rho\mathcal{D}$)
Sh	Sherwood number averaged over both channel walls ($\equiv kh/\mathcal{D}$)
SKA	specific volumetric mass transfer coefficient in the channel (s^{-1})
SPC	specific cross-flow power consumption in the channel (W/m^3)
u	superficial velocity in the channel (m/s)
w	width of the measuring cell (m)

Greek letters

α	flow attack angle
β	angle between crossing filaments
μ	dynamic viscosity of the solution (Pa s)
ρ	density of the solution (kg/m^3)
Φ_v	volumetric flow rate through the channel (m^3/s)

References

[1] G. Schock, A. Miquel, Mass transfer and pressure loss in spiral wound modules, Desalination 64 (1987) 339–352.
[2] Y. Winograd, A. Solan, M. Toren, Mass transfer in narrow channels in the presence of turbulence promoters, Desalination 13 (1973) 171–186.
[3] M.J. van der Waal, I.G. Racz, Mass transfer in corrugated-plate membrane modules. I. Hyperfiltration experiments, J. Membr. Sci. 40 (1989) 243–260.
[4] H.M. Yeh, K.T. Chen, Improvement of ultrafiltration performance in tubular membranes using a twisted wire-rod assembly, J. Membr. Sci. 178 (2000) 43–53.
[5] P. Feron, Hydrodynamics and mass transfer in obstructed narrow channels, Ph.D. Thesis, Cranfield Institute of Technology, 1991.
[6] A.R. Da Costa, A.G. Fane, C.J.D. Fell, A.C.M. Franken, Optimal channel spacer design for ultrafiltration, J. Membr. Sci. 62 (1991) 275–291.
[7] B.B. Gupta, J.A. Howell, D. Wu, R.W. Field, A helical baffle for cross flow microfiltration, J. Membr. Sci. 99 (1995) 31–42.
[8] A.R. Da Costa, A.G. Fane, D.E. Wiley, Spacer characterization and pressure drop modeling in spacer-filled channels for ultrafiltration, J. Membr. Sci. 87 (1994) 79–98.
[9] J.J.S. Shen, R.F. Probstein, Turbulence promotion and hydrodynamic optimization in an ultrafiltration process, Ind. Eng. Chem. Process Des. Develop. 18 (1979) 547–554.
[10] Z. Cao, D.E. Wiley, A.G. Fane, CFD simulation of net-type turbulence promoters in a narrow channel, J. Membr. Sci. 185 (2001) 157–176.

[11] S.K. Karode, A. Kumar, Flow visualization through spacer filled channels by computational fluid dynamics. I. Pressure drop and shear rate calculations for flat sheet geometry, J. Membr. Sci. 193 (2001) 69–84.
[12] G. Costigan, B.J. Bellhouse, C. Picard, Flux enhancement in microfiltration by corkscrew vortices formed in helical flow passages, J. Membr. Sci. 206 (2002) 179–188.
[13] V. Geralds, V. Semiao, M.N. de Pinho, Flow management in nanofiltration spiral wound modules with ladder-type spacers, J. Membr. Sci. 203 (2002) 87–102.
[14] F. Li, W. Meindersma, A.B. de Haan, T. Reith, Optimization of net spacers in spiral wound membrane modules, J. Membr. Sci. 208 (2002) 289–302.
[15] J.H. Ferziger, M. Peric, Computational Methods for Fluid Dynamics, 2nd ed., Springer, Berlin, 1999.
[16] R. Rautenbach, R. Albrecht, Membrane Processes, Wiley, New York, 1981.
[17] J.R. Selman, C.W. Tobias, Mass transfer measurements by the limiting current technique, in: Advances in Chemical Engineering, vol. 10, Academic Press, New York, 1978, pp. 211–318.
[18] H. Futselaar, The transverse flow membrane module, Ph.D. Thesis, University of Twente, Enschede, The Netherlands, 1993.
[19] P. Moulin, The use of Dean vortices to improve mass transfer in membrane separation processes, Ph.D. Thesis, University Paul Sabatier de Toulouse, Toulouse, 1996.
[20] G. Prentice, Electrochemical Engineering Principles, Prentice-Hall, Englewood Cliffs, NJ, 1991.
[21] D.W. Hubbard, E.N. Lightfoot, Correlation of heat and mass transfer data for high Schmidt and Reynolds numbers, I&EC Fund. 5 (1966) 370–379.
[22] F.P. Berger, A. Ziai, Optimization of experimental conditions for electrochemical mass transfer measurements, Chem. Eng. Res. Des. 61 (1983) 377–382.
[23] T. Mizushina, The electrochemical method in transport phenomena, Adv. Heat Transfer 7 (1971) 87–161.
[24] P. Van Shaw, L.P. Reiss, T.J. Hanratty, Rates of turbulent transfer to a pipe wall in the mass transfer entry region, AIChE J. 9 (1963) 362–364.
[25] C.F. Oduoza, A.A. Wragg, M.A. Patrick, The effects of a variety of wall obstructions on local mass transfer in a parallel plate electrochemical flow cell, Chem. Eng. J. 68 (1997) 145–155.
[26] S.L. Gordon, J.S. Newman, C.W. Tobias, Berichte der Bunsengesellschaft 70 (1966) 414–420.
[27] M. Gerritsjans, Verbetering van de stofoverdracht in membraanmodules, Thesis, University of Twente, 1998.
[28] V.S. Minnikanti, S. DasGupta, S. De, Prediction of mass transfer coefficient with suction for turbulent flow in cross-flow ultrafiltration, J. Membr. Sci. 157 (1999) 227–239.
[29] S. De, P.K. Bhattacharya, Prediction of mass-transfer coefficient with suction in the applications of reverse osmosis and ultrafiltration, J. Membr. Sci. 128 (1997) 119–131.
[30] J.W. van Heuven, Report No. R 2000/390, The Netherlands Organisation for Applied Research, December 2000 (Appendix 7).
[31] M. Zlokarnik, Dimensional Analysis and Scale-up in Chemical Engineering, Springer, Berlin, 1991.
[32] G. Belfort, G.A. Guter, An experimental study of electrodialysis hydrodynamics, Desalination 10 (1972) 221–262.
[33] W.J. Beek, K.M.K. Muttzall, J.W. van Heuven, Transport Phenomena, Wiley, New York, 1999.
[34] R.B. Bird, W.E. Stewart, E.N. Lightfoot, Transport Phenomena, Wiley, New York, 1962.